Numerical and Experimental Investigation of the Reduction of Hypersonic Nose Tip Ablation

Sidra I. Silton[*] and David B. Goldstein[†]
Center for Aeromechanics Research
Department of Aerospace Engineering & Engineering Mechanics
The University of Texas at Austin
Austin, TX 78712-1085

Abstract

To reduce the severe heating and ablation at the nose tip of a hypersonic vehicle, the introduction of a forward-facing cavity into the nose tip is explored. In the present joint numerical/experimental study, the effects of the cavity on ablation are explicitly addressed whereas previous studies have concentrated on heating rates alone. While the study is continuing, initial results look promising. Numerical and experimental results agree surprisingly well for a baseline hemisphere cylinder case.

1 Introduction

Hypersonic vehicles travel at such high velocities that severe heating and shape changes due to ablation may occur. These shape changes may need to be minimized as they can produce unacceptable perturbations in the aerodynamics and, therefore, the flight path. The heat loads and material ablation that lead to the shape changes are most critical at the nose tip. To this end, it is desirable to find ways to delay the onset of ablation, decrease the rate of ablation, or devise a way to ensure ablation is uniform.

The introduction of a forward-facing cavity into the nose tip of a hypersonic projectile (fig. 1) has recently been found to reduce local heating over the entire nose region compared to that of a similar spherical nose tip. A range of cavity geometries that are effective in decreasing the heating rate has been explored. However, the effects of introducing a forward-facing cavity on ablation have not been directly addressed.

Preliminary experiments, using an infrared (IR) camera, by Yuceil et al. [11] indicated that large diameter, shallow cavities (length-to-diameter ratio (L/D) between 0.15 and 0.35) created a stable 'cool ring', just outside of a sharp cavity lip, with temperatures locally lower than those found on a simple spherical nose. A joint numerical and experimental study by Engblom et al.
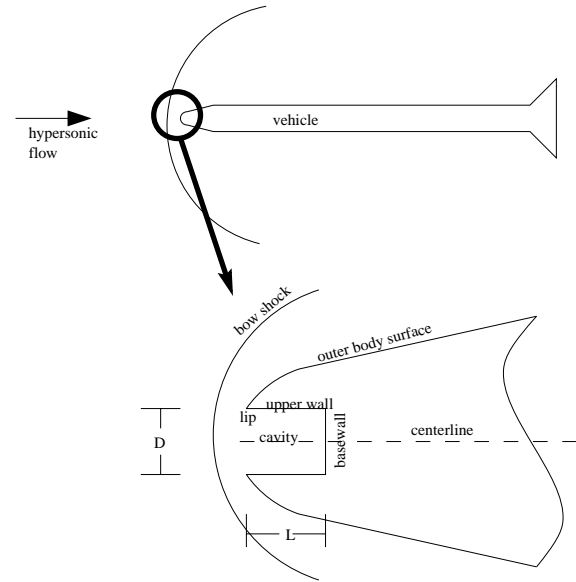

Figure 1: Schematic of axial forward-facing cavity in the nose region of a hypersonic vehicle. [4]

[3] concluded that sharp cavity lips produce not only a separated recirculation region (accounting for the 'cool ring') but also severe heating just inside the cavity for weakly oscillating flows. In time-accurate numerical simulations by Engblom et al. [2], it was found that resonant oscillations were obtained if either freestream fluctuations were present or a sufficiently deep cavity was employed. Yuceil [13] reported experimental results for a deep cavity of L/D=2.0 for which he found substantial cooling over the entire nose region as compared to the case with no cavity. Engblom and Goldstein [1] showed that the local heat flux everywhere on the surface was reduced when strong longitudinal pressure oscillations within the cavity induced large bow shock oscillations. That numerical effort also found that the heat reduction benefit appeared to increase with mean relative bow shock speed. The reader is refered specifically to the paper by Engblom and Goldstein [1] for a detailed discussion of the heat flux reduction mechanisms.

The present paper presents results from a joint numerical/experimental study of the effects of a forward-facing cavity on the ablation of a nose tip in hypersonic flow. There were three objectives for this study: 1) to attempt

---

[*] Graduate Research Assistant, Student Member AIAA
[†] Assistant Professor, Senior Member AIAA

to confirm, numerically and experimentally, that the introduction of a forward-facing cavity into a hypersonic projectile reduces the ablation of the nose region, 2) to develop a viable experimental technique for studying ablation in the University of Texas at Austin J.J. Pickle Research Center (PRC) facility, since the facility is not a high enthalpy tunnel, and 3) to validate the further use of the computational model for the determination of ablation onset time.

Section 2 discusses the computational modeling used with particular emphasis on the joint solution of the flowfield and solid body temperature field. Section 3 contains an overview of the experimental setup and procedure. The results found in Section 4 are broken into the computational findings (sec. 4.1) and the experimental findings (sec. 4.2).

2   Numerical Methodology

2.1   Computer Code Description

The commercial computer code, INCA (licensed from Amtec Engineering), was used for this study. INCA is a finite-volume code that utilizes flux splitting with upwinding to capture strong shocks. Fluxes are computed with the flux splitting of Steger and Warming. INCA offers an efficient Lower-Upper Successive Gauss-Seidel (LU-SGS) implicit solver to calculate steady flowfields. The LU-SGS algorithm approximately solves the system of equations using two sweeps of a point Gauss-Seidel relaxation. INCA offers a variation of the LU-SGS implicit solver to calculate unsteady flows which was utilized in the present work. This algorithm permits much larger time steps than a simple Euler step method by performing a sufficient number of sub-iterations at each time step. This algorithm is also second-order accurate in time.

The heat conduction module of INCA allows for the solid body heat conduction problem to be solved in a time accurate manner using a variation of the LU-SGS algorithm used to calculate the flowfield. Because of the different time scales involved in the flowfield solution and the solid body heat conduction problem, a completely coupled solution was not suitable for the present problem. A pseudo-coupling process described in Section 2.3 appears to generate reasonable solutions within a practicable amount of CPU time.

All grid generation for this study (flowfield and solid body) is performed using GRIDALL (Amtec Engineering) to create algebraic grids. The baseline numerical nose tip was modeled as a hemispherically blunted cylinder. The nose-cavity tip was modeled as a hemispherically blunted cylinder containing an axial, cylindrical cavity.

A single grid was generated for the baseline (no cavity) flowfield case (fig. 2). A two zone grid with an infinitely sharp lip (fig. 3) was used for one of the cavity cases where one zone encompassed only the cavity. A four zone grid with a rounded lip (fig. 4) was used for the other cavity case. Four zones were needed in order to maintain grid quality and resolution near the lip and shock regions. One zone encompassed only the area around the lip (zone 1). A second zone (zone 2) was used to extend this area to the outflow boundary. Zones 3 and 4 contained the cavity and the remainder of the flowfield, respectively. This grid organization was appropriate because the bow shock typically oscillates axially, remaining fairly well aligned with the grid. The zones near the lip are chosen such that the bow shock would not cross the zone boundaries. For the solid bodies in the baseline and cavity cases, two-zone grids were generated (figs. 5 (a) and (b), respectively). Note, INCA does not currently support localized grid refinement (i.e., a cell face must contact only one other cell face), thus limiting structured grid capability.
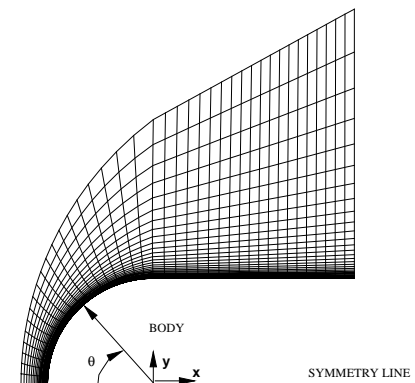

Figure 2: Schematic of the single zone flowfield grid used for baseline calculations. Actual surface spacing at the stagnation point was $5.0 \times 10^{-4} mm$.

2.2   Numerical Assumptions

Body geometry and material properties and freestream conditions are consistent with those of the experiments described in section 3. The freestream static air pressure and temperature was set at 4694 Pa and 64 K, respectively, corresponding to an isentropic stagnation pressure and temperature of $2.275 MPa$ and $370 K$, respectively. The freestream velocity was set at $787 m/s$, corresponding to Mach 4.92 and a freestream Reynolds number of $5.0 \times 10^5 cm^{-1}$.

Schematics for the hemisphere-cylinder geometries, with and without a cylindrical cavity used in the numerical simulations are shown in figure 6. The numerical body
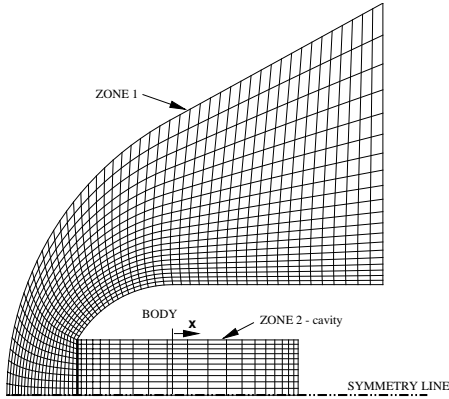
Figure 3: Schematic of the flowfield grid used for L/D=2.0 sharp lip calculations. Actual surface spacing everywhere was $2.5 \times 10^{-4} mm$.
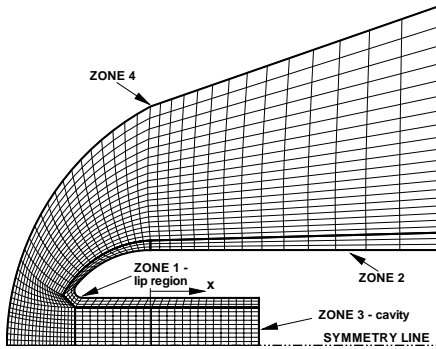

Figure 4: Schematic of the flowfield grid used for L/D=2.0 rounded lip calculations. Actual surface spacing at cavity base wall was $1.0 \times 10^{-1} mm$ while surface spacing everywhere else was $9.05 \times 10^{-4} mm$.
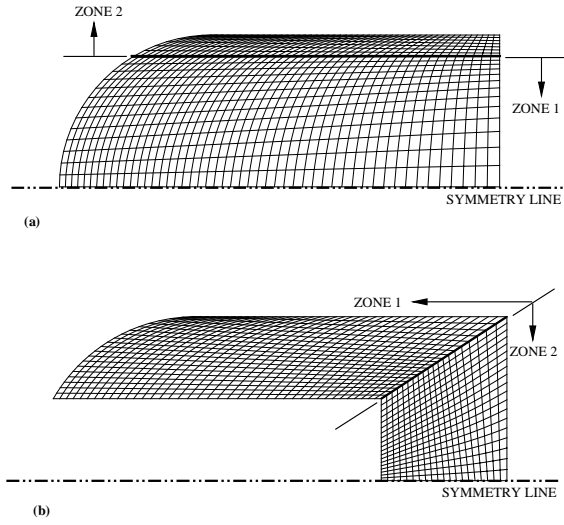

Figure 5: Representative solid body two zone grids for (a) baseline case and (b) sharp lip cavity case. (rounded lip geometry not shown)

diameter, D_n, was $2.54 cm$. For the case with a cavity, the cavity diameter, D, was $1.27 cm$ and the cavity length, L, was $2.54 cm$ measured from the cavity lip to the cavity base. The models included an infinitely sharp cavity lip, which is a close emulation of one experiment, and a rounded cavity lip ($1.0 mm$ lip), which approximates the rounded lip of the second and third experimental models.
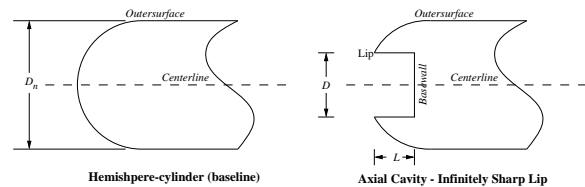

Figure 6: Nose-cavity geometries used in numerical simulations. (rounded lip geometry not shown)

The material properties of the body were assumed to be those of the low temperature ablator chosen for the experiment, water ice. Water ice,was chosen for the reasons explained in section 3.2. The material properties of density, specific heat and thermal conductivity, are specified, as obtained from Mills [8] at $273 K$ are $910 kg/m^3$, $1930 J/kgK$, and $2.22 W/mK$, respectively. These constant property values were used, although temperatures spanned a wide range, since INCA cannot yet handle variable properties. The effect that specifying constant property values had on the results was not explored in the present work. However, it was believed that the introduction of variable material property values would lead to

3

greater consistency with experiments.

A number of other simplifying assumptions were made in the simulations. First, a thermally and calorically perfect gas was assumed. Therefore, the transport properties, viscosity (μ) and thermal conductivity (k), were calculated as functions of temperature only. Also, the flow was assumed axisymmetric. This was appropriate because the bow shock had been found to oscillate axisymmetrically in front of deep cavities in previous experiments [13]. Pressure oscillations at the cavity base were also found to be planar in experiments [13, 14, 3], again indicating axisymmetric flow. Laminar flow was assumed due to the small scale of the flowfield (i.e., the nose region). Due to low speed flow in the stagnation region, the Reynolds number per centimeter was much smaller along the body surface inside the cavity and outside the cavity near the lip than the freestream Reynolds number ($5.0 \times 10^5 cm^{-1}$). The characteristic flow lengths were less than one centimeter and a favorable pressure gradient was present along the cavity wall in steady flow. Therefore, transition might not be expected to occur within regions of interest inside the cavity and downstream of the re-attachment point outside the lip unless the flow is 'tripped' by the oscillations within the cavity.

The adequacy of these assumptions will be re-evaluated in light of both the numerical and experimental results.

2.3 Numerical Procedure

Due to the much shorter characteristic times in the oscillating flowfield (O($1/3000s$)) than in the solid body heat conduction (O($1s$)), it was not practical to try to solve the two parts of the problem simultaneously as a few seconds were required for the stagnation point of the solid body to begin to warm. For this reason, the pseudo-coupling procedure, discussed below, was developed. The procedures for obtaining the required inputs for the heat conduction code are slightly different for the baseline case and the cavity cases. For this reason, the procedures are discussed separately.

2.3.1 Baseline Procedure

The output files from the steady flowfield solution were used to obtain the heat flux distribution, $q(\theta)$, over the solid body. The heat flux distribution was then used to calculate the heat conduction coefficient, $h(\theta)$, as

$$q = h(T_w - T_{aw}) \qquad (1)$$

where T_{aw} was the adiabatic wall temperature and T_w was the solid body wall temperature. The adiabatic wall temperature was determined by computing a second flowfield solution assuming an adiabatic wall boundary condition. These data were input into the heat conduction code to obtain a new wall temperature distribution at time $t + \Delta t$, $T_w(\theta, t + \Delta t)$, as described below in the heat conduction code procedure. A new steady flowfield solution was then calculated using the wall temperature distribution, $T_w(\theta, t + \Delta t)$, returned from the heat conduction code. This process was repeated until the stagnation point (the point of highest heating) had reached its melting point. The calculations were ended at this point because the shape change, due to ablation, could not be computed by the code.

2.3.2 Cavity Procedure

When an axial cavity of L/D = 2.0 was introduced into the nose of a projectile, the bow shock oscillations were self-sustaining [4]. Due to this phenomenon, the flowfield had to be numerically solved in a time-accurate manner.

The restart file from the pseudo-steady flowfield solution (constant amplitude base pressure oscillations) was utilized to generate a time-accurate solution of the flowfield and the corresponding surface heat flux distribution. This was done by initially assuming that the solid body was isothermal at its initial temperature. Generally, one pressure oscillation cycle was solved using 4000 global time steps and 6 sub-iterations per time step. The corresponding CPU time requirement (at the highest spatial resolution) was typically 38 hours/cycle on a CRAY J90. The solution was assumed converged once the mean heat flux distribution did not change appreciably from one cycle to the next. The mean heat flux distribution was obtained by averaging the surface heat fluxes over one complete cycle using 50 realizations in time at each point along the body surface [4]. The mean surface heat flux distribution was then taken as the surface heat flux distribution for that surface temperature distribution (initially the surface temperature was constant).

This mean heat flux distribution was used to obtain the heat conduction coefficient distribution using equation (1) where T_{aw} was the forced-steady adiabatic wall temperature and T_w was the mean wall temperature during the cycle. As for the baseline case, the forced-steady adiabatic wall temperature was determined by computing a steady flowfield solution assuming an adiabatic wall boundary condition. A steady flowfield solution was forced for this case by using large implicit time steps without sub-iterations. Although this T_{aw} distribution was not as accurate as if the mean adiabatic wall temperature over one pressure cycle was utilized, the forced-steady adiabatic wall temperature was believed to give a reasonable result while requiring much less computing time. A new wall temperature distribution was then determined as described below and used as the fixed wall boundary condition in the next iteration of the flow field solution. The entire process was repeated until some point on the outside of the body had reached its melting temperature.

2.3.3 Heat Conduction Code Procedure

The heat conduction coefficient distribution obtained from the flow solver as described above was used as the boundary condition for the heat conduction code. The heat conduction code was then run from time t, the point in time at which the previous wall temperature distribution was determined. The heat conduction solution was obtained using a time step of $1.0 \times 10^{-4}s$ with 15 sub-iterations. For the baseline case, the CPU time to obtain a solution to $t = 5s$ was typically 24 hours on a DEC Alpha. The corresponding CPU time to obtain a solution to $t = 2s$ for the sharp lip cavity case was typically 30 hours due to a more refined grid being utilized.

A reference temperature distribution equal to that of the (forced-steady) adiabatic wall temperature distribution was always utilized. When a temperature change of a predetermined amount in the region of peak heating has occurred (say, 10%), a new wall temperature distribution was extracted from the output files and input into the flow solver as the new fixed wall temperature distribution.

2.3.4 Grid Resolution

A grid refinement study was conducted for each case to determine the maximum tolerable surface cell thickness near the stagnation region for the baseline case and in the cavity lip region for the cavity cases. Details of the grid resolution studies can be found in section 4.1.

3 Experimental Methodology

All experiments were conducted in the Mach 5 blowdown wind tunnel of the Wind Tunnel Laboratories located at PRC. The wind tunnel (including flow conditions) will be discussed in section 3.1 and the model will be described in 3.2.

3.1 Wind Tunnel

The Mach 5 tunnel has a rectangular test section $15.24cm$ ($6.00in.$) wide, $17.78cm$ ($7.00in.$) high, and $68.58cm$ ($27.00in$) long. It has a floor slot that was used to mount the models, and circular side-wall windows for video and photography. Compressed air (stored at $17.24MPa$ ($2500psia$) in four external tanks with a total volume of $3.964m^3$ ($140ft^3$)) allowed for run times of up to one minute without a significant drop in the tunnel stagnation pressure. The incoming air was heated by two banks of nichrome wire resistive heaters ($420kW$ each) located upstream of the stagnation chamber.

The tunnel was operated at a nominal stagnation pressure and temperature of $2.30MPa$ ($333psia$) and $370K$ ($666°R$), respectively. At the freestream Mach number of 4.92, these stagnation conditions lead to a freestream unit Reynolds number of $5.0 \times 10^5 cm^{-1}$ ($1.52 \times 10^7 ft^{-1}$) and a freestream velocity of $787m/s$ ($2575ft/s$).

3.2 Models

A missile nose is typically a blunted cone-cylinder configuration. However, since the focus of this work was on the stagnation region, the missile nose was modeled as a sphere-cylinder as done previously by Farnsworth [5], Yuceil [13], and Engblom [4]. Therefore, the basic model geometry is a hemispherically-blunted cylinder with a streamwise circular nose cavity.

The material chosen for the model needed to ablate at low temperatures, as the stagnation temperature of the wind tunnel (T_{stag}) was considerably lower than that in actual flight. Water ice was chosen as a suitable material because it was cheap, well-characterized, and neither toxic, flammable, nor corrosive. Ice also has a very low sublimation rate (low vapor pressure) at low temperatures. Ice has a melting, or (in this case) ablation, temperature of $273K$ ($492.67°R$), nearly $100K$ below T_{stag}. In order to delay the onset of ablation for several seconds into the tunnel run and to establish a definite initial temperature, the ice was initially cooled to liquid nitrogen (LN2) temperature ($78K$).

Several models were used over the course of the study. Each ice model was frozen in a mold (fig. 7(b)) which was polished smooth with 1000 grit sand paper. The mold created a model with a nose diameter, D_n, of $2.54cm$ ($1in.$). Different cavity depths, L, were obtained by fixing an insert in the mold at the required location during the freezing process. One insert had a $1.27cm$ ($0.5in.$) radius of curvature, equal to that of the nose, which ensured that a spherical nose was obtained for the baseline case (i.e. L = 0). The other insert had a flat bottom in order to produce a flat bottom cavity when cavity depths greater than zero were desired. A cavity diameter of one half the model nose diameter ($D = 1.27cm$ ($0.5in.$)) was chosen.

The mold, lightly coated with Pam vegetable oil spray to assist in the removal of the ice, was filled with distilled water. Fiberglass threads were added in order to strengthen the model. Without the addition of the fiberglass, the ice would shatter during tunnel startup. The mass of fiberglass added ($\ll 1g$) was not a significant fraction of the total mass of the ice and was not believed to have changed the thermal characteristics of the ice but instead did produce a tough and viable fiber re-enforced composite.

After the fiberglass had been stirred into the water, a brass spindle (fig. 7(a)) was placed in the aluminum mold (fig. 7(b)). The spindle was used to extract the model from the mold and was the base on which to attach the model to
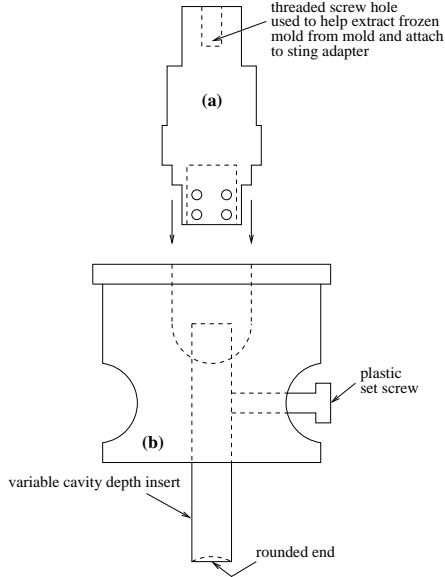
Figure 7: (a) Spindle and (b) mold used to create ice models for experiment.

the sting adapter (and sting) (fig. 8, as indicated). Holes were drilled into the portion of the spindle that the ice would form around (the cup) so water would be present on both the interior and the exterior of the cup. This insured that for the runs in which a cavity was used, the interior of the cavity would be fully covered with ice. The entire mold was then placed in LN2 vapors (a few inches above a pool of LN2) for 20 minutes until the water was completely frozen. The spindle with the ice model attached was then forcibly pulled free of the mold. For rounded lip models, the ice cavity lip was smoothed with sandpaper to approximately the desired radius. This was accomplished by hand with the frozen spindle held by hand or in a drill press. The spindle, with the completed ice model attached, was then placed back in the LN2 vapors for one to two hours more in order to gradually reduce the temperature of the ice to $78K$.

3.2.1 Model Shielding

Shielding of the model was required in the present study in order to protect the model from heating during startup of the wind tunnel. The shield consisted of two parts, one reusable (outer shroud), the other expendable (shroud cap) (fig. 8, as indicated).

The outer shroud, which fit over the spindle, consisted of a hollow brass cylinder with a brass flange attached to one end. Brass was chosen as the material for the shielding in order to match the thermal expansion of the spindle and help reduce any sticking of the shield to the spindle. The outer shroud was kept in place with a long threaded
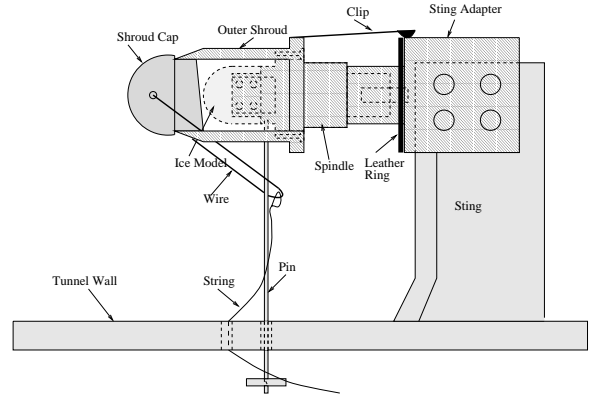

Figure 8: Schematic representation of wind tunnel mounted model during tunnel startup while ice is protected.

pin that went through the shroud and into a threaded hole in the bottom of the spindle. This pin was fitted up through the tunnel floor so that it could be removed after the tunnel had reached steady-state conditions (15-20 seconds into the run). The outer shroud was designed such that aerodynamic forces would push it back over the spindle after the pin was removed. A spring metal clip kept the outer shroud in contact with the sting adapter for the remainder of the run.

The shroud cap was a wooden plug that fit into the outer shroud and covered the ice. A low-density pine wood was used so as not to damage the facility and to have a material with a low thermal conductivity. Once the pin was removed and the outer shroud began to slide back, the shroud cap came loose and flew off downstream due to the unbalanced pressure forces acting on it. The shroud cap was kept in place during startup by placing a wire through the bottom of the plug and wrapping the wire around the pin, which held the shroud in place.

Although no tests were conducted to determine the nose temperature rise during startup, the shield was assumed to provide sufficient insulation of the model from the flowfield because there was no direct contact between the shield and the ice. The shield did fail on occasion for two main reasons: the shroud cap came out before steady-state conditions were reached or the outer shroud did not slide back even after the pin was removed (a problem of sliding contact at $78K$).

3.3 Experimental Procedure

3.3.1 Final Model Preparation

Prior to each run, the interior of the outer shroud was coated with graphite powder and placed in LN2 to cool. Once the LN2 stopped boiling, the outer shroud was removed from the LN2, but not from the vapors. The outer shroud was positioned over the ice model and spindle (the spindle was

also coated with graphite powder) and pinned in place with a short screw. The entire assembly was again submerged in the LN2 in order to again cool the ice model to 78K. Once the assembly cooled, it was mounted in the wind tunnel test section by screwing the spindle into the sting adapter. The shroud cap was put into place and the short screw was replaced with the pin (fig. 8). In order to minimize heating of the spindle during this time and to prevent the accumulation of frost, the sting extender was precooled with LN2, the back flow into the tunnel was blocked with paper, and the air conditioning was used to dehumidify the room.

3.3.2 Ice Exposure

Once conditions in the wind tunnel stabilized, the pin holding the shield in place was removed allowing the outer shroud to slide back over the spindle and expose the ice model to freestream conditions (fig. 9). The time at which the model became exposed to freestream conditions was considered time zero although images have been taken prior to this time.
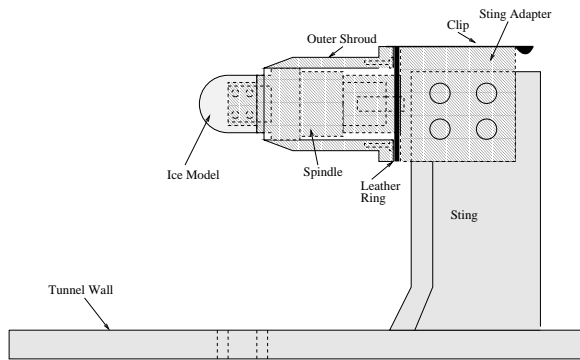

Figure 9: Schematic of exposed wind tunnel model after tunnel startup is complete.

3.3.3 Video Imaging Process

A Panasonic WV-3250 video camera with horizontal resolution of 350 lines at center was used to collect the needed data. The camera scanned 525 lines with a framing rate of 30 Hz. The video camera began recording prior to the start of the wind tunnel so that removal of the shield was captured. The timer on the video camera was utilized in order to determine at what time the shield was removed, how long after this time ablation began to occur, and how quickly the material ablated. The video camera was set perpendicular to the circular viewing window. Due to the positioning of the video camera, little of the interior of the cavity could be visualized. The model was illuminated with a high intensity photographer's light. To minimize any radiative heating of the model due to the light, the circular

viewing window was covered until just prior to the tunnel start.

The video images were digitized with the Macintosh Movie Player during post-processing. Once on the computer, digitized images were extracted at one-second intervals during the run in order to obtain still images for comparison between runs. The still images were transferred to individual files for later use.

3.3.4 Analysis Techniques

For each still image, the pixel location of the most forward position of the model could be determined. Using a reference location in the image allowed the measurement of a nose position versus time for each run. A least squares fitted line could then be calculated for each run. The slope of this line determined the average recession rate for that run. When repeated runs were conducted for a given geometry, the recession rates were averaged.

4 Results

The numerical and experimental results are presented below in sections 4.1 and 4.2, respectively. Each section is subdivided into the specific geometrical cases that were investigated, i.e. baseline, deep cavity, etc.

4.1 Numerical Results

In the baseline simulation, it was assumed that the stagnation point was the point of highest heating and would therefore be the first to reach the melting temperature. For the L/D=2.0 simulations, the point of highest heating had to first be determined. That point was then used as the object of study.

4.1.1 Baseline Case

In order to ensure convergence of the calculated surface heat flux distributions, a grid refinement study was conducted. Surface heat flux distributions were obtained for a steady flowfield around the baseline body assuming an isothermal wall boundary condition of $100\,K$, the initial temperature of the ice model assuming some model warming prior to exposure to the free stream. Of the four grids studied, three contained 120 points along the surface body; the fourth contained 80 points. This spatial decomposition adequately resolved the flowfield. However, the number of points used along the body was increased further to 200 when the heat conduction code was being utilized as the interior body cells and the flowfield cells must match up on the body surface. The fineness level of the grid near the wall (i.e. surface cell thickness and the number of grid cells

near the wall) was varied for the four grids studied from $1.27 \times 10^{-2} mm$ to $1.0 \times 10^{-4} mm$. Each grid contained between 80 and 180 cells 'normal' to the wall depending on the surface cell fineness. Surface heat flux distributions for each of the four grids are shown in figure 10. Convergence was obtained everywhere along the surface for the grid with a surface cell thickness of $5.0 \times 10^{-4} mm$ as demonstrated by the coincidence of the $5.0 \times 10^{-4} mm$ and the $1.0 \times 10^{-4} mm$ curves. Also, note the agreement with the Fay and Riddell [6] value for peak heating at the nose of $268 \, kW/m^2$.
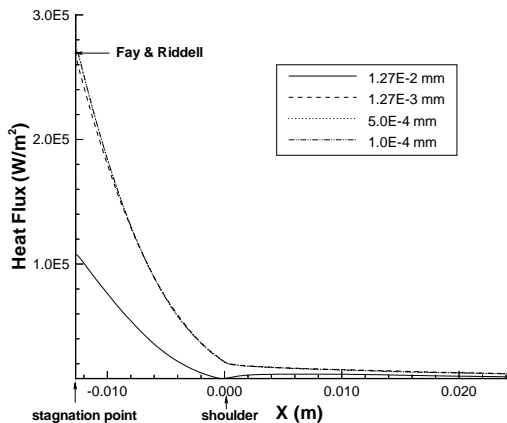

Figure 10: Surface heat flux distribution over baseline blunt body for various surface grid fineness levels. Body was isothermal at $100 K$.

Temporal resolution for the heat conduction zone was ensured by comparing the stagnation point temperature history (i.e. how it changed over time) with another history obtained using finer resolution in time. Each time step used 15 sub-iterations. The heat conduction coefficient distribution used was calculated from equation (1) with an unconverged surface heat flux distribution for the initial wall temperature ($q(\theta, 100K)$) and the free stream stagnation temperature (instead of adiabatic wall temperature) used as the reference temperature. This convergence study was believed to be adequate because the same q and T_{aw} were used for each case. Stagnation point temperature histories calculated using these heat conduction coefficient distribution and various time steps are shown in figure 11. Sufficient temporal convergence is seen to be obtained for the time step of $1.0 \times 10^{-4} s$ as demonstrated by the coincidence of the $1.0 \times 10^{-4} s$ and the $5.0 \times 10^{-5} s$ curves.

The results of this spatial resolution study ($\Delta x_{min} = 5.0 \times 10^{-4} mm$) were then used to obtain the desired surface heat flux distributions, $q(\theta, T_w)$. The heat conduction coefficient distributions, $h(\theta, T_w)$, were obtained from the surface heat flux distributions using equation (1) and were
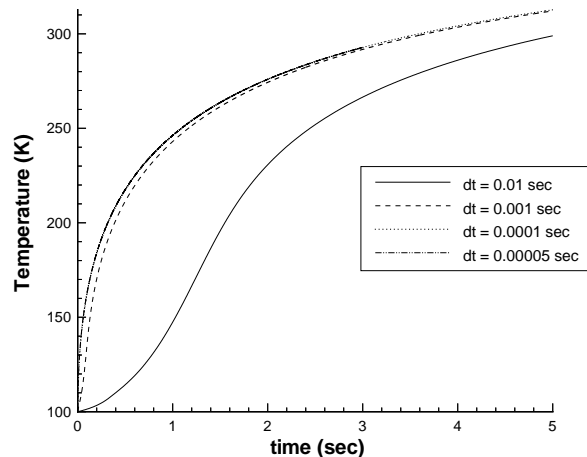

Figure 11: Stagnation point temperature histories of baseline case for various time steps.

used as input into the heat conduction code. Four different heat conduction coefficient distributions were examined: $h(\theta, T_w)$ evaluated at $T_w = 100K$, $T_w = 186K$, and $T_w = 273K$ and an average h, $h(\theta, avg)$ calculated from $h(\theta, 100K)$ and $h(\theta, 273K)$ by

$$h(\theta, avg) = \frac{h(\theta, 100K) + h(\theta, 273K)}{2} \qquad (2)$$

Assuming constant $h(\theta, T_w)$ or $h(\theta, avg)$ in time for each case, the heat conduction code was run from an initial body temperature of $100K$ ($t = 0s$) until $t = 5s$ at which time the temperature of the stagnation point exceeded $273K$.

A comparison of the stagnation point temperature histories for the four cases (fig. 12) indicates essentially the same time (~ 4 sec) for the stagnation point to begin melting regardless of how $h(\theta, T_w)$ was determined. Also included in figure 12 is a two iteration case and a four iteration case (process as described in sec. 2.3) which utilize the $h(\theta, 100K)$ distribution in the heat conduction code until a stagnation temperature of approximately $186.5K$ or $143.25K$ was reached, respectively. Table 1 indicates the actual time at which the stagnation point reached $273K$ for all six cases. The time at which the stagnation point began to melt did not vary by more 4 percent among all six cases. Therefore, it was concluded that more than four iterations were not necessary to obtain results for the baseline case. In fact, it hardly matters which $h(\theta)$ distribution is used.

4.1.2 Cavity Case

The results for the cavity case are broken into the infinitely sharp lip and the rounded lip cases for ease of discussion.
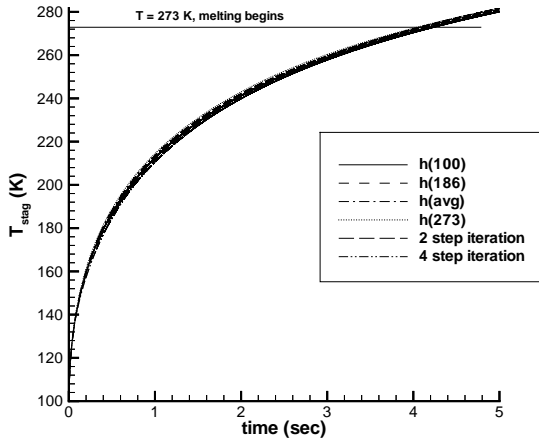
Figure 12: Stagnation point temperature histories for various heat conduction coefficient distributions, $h(\theta, T)$.

distribution	time (sec)
$h(\theta, 100K)$	4.20
$h(\theta, avg)$	4.12
$h(\theta, avg)$	4.22
$h(\theta, 273K)$	4.05
two iteration	4.25
four iteration	4.09

Table 1: Actual times at which the stagnation point temperature reached $273K$ for each heat conduction coefficient distribution used.

Only partial solutions are available at this time due difficulties with the INCA code.

4.1.2.1 Infinitely Sharp Lip Simulation The flowfield simulation was first performed using a coarse grid (surface spacing of $1.0 \times 10^{-3}mm$) and 1000 time steps per cycle until a pseudo-steady oscillating solution was reached. The simulation was considered pseudo-steady once the mean surface heat flux distribution and base pressure level did not change appreciably for several consecutive cycles. A portion of the time accurate results for the pressure history at the base of the cavity is presented in figure 13. It is seen that the primary mode frequency was approximately 3000 Hz. The oscillations were self-sustained as expected for this cavity geometry [3].

An extensive temporal and spatial resolution parameter study (isothermal wall at $100K$) was then conducted to confirm that the heat flux was indeed converged. The temporal resolution study was conducted first. Mean heat flux distributions for one pressure cycle were computed for var-
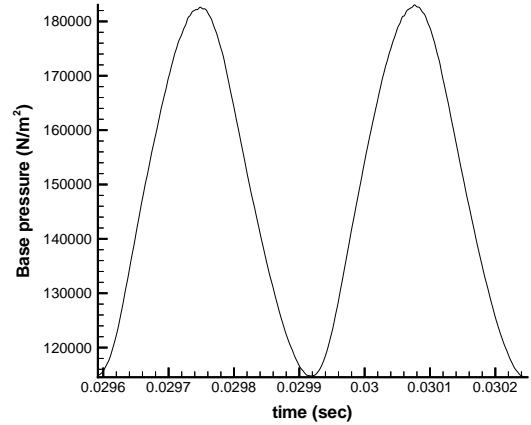

Figure 13: Segment of base pressure history for sharp lip cavity.

ious numbers of time steps per cycle. Results of this study for the outer portion of the body (fig. 14) showed reasonable temporal convergence when 4000 time steps per cycle were used although 3000 or even 2000 would also have been adequate.
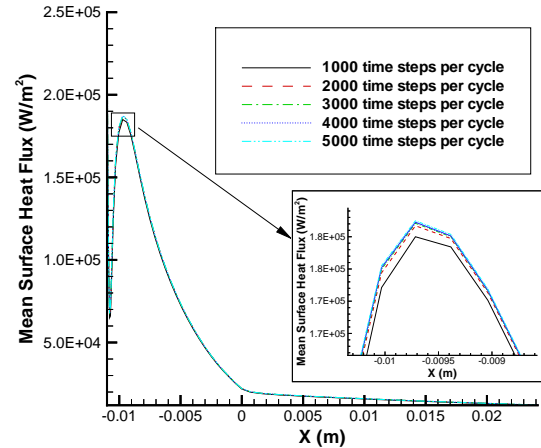

Figure 14: Mean heat flux distribution on outside of body for various number of time steps per cycle to determine temporal convergence. (6 sub-iterations per time step)

Spatial resolution was then verified using 4000 time steps per cycle and increasing grid fineness along the wall. Of the five grids studied, four contained 300 cells along the outer surface body and 399 cells 'normal' to the wall; the fifth and coarsest grid contained 100 points in each direction. To resolve the cavity adequately, the coarsest grid contained 140 cells up from the line of symmetry and 45

9

cells from the cavity base wall to the cavity lip. The four other fine grids contained 200 cells up from the line of symmetry and 99 cells from the cavity base wall to the cavity lip. This fine spatial decomposition adequately resolved the flowfield and also resolved the solid body for the heat conduction calculations. Again, recall that the interior body cells and the flowfield cells must match up on the body surface.

The fineness level of the grid near the wall (i.e. surface cell thickness and the number of grid cells near the wall) was varied for the five grids studied from $1.0 \times 10^{-3}mm$ (coarse cell distribution) to $1.0 \times 10^{-4}mm$. As resolution near the wall was increased, more small fluctuations in heat flux occurred (most likely due to the solution capturing a greater number of small lip eddies). In order to work around this phenomenon so that computational times remained finite, the area around the reattachment shock (fig. 15), where peak heating occurs, was more closely examined. Comparing the mean surface heat flux distributions at the wall for the grids (fig. 16), a surface spacing of $2.5 \times 10^{-4}mm$ was considered converged since there was very little difference between it and a surface spacing of $5.0 \times 10^{-4}mm$. If spacing is reduced further to $1.0 \times 10^{-4}mm$, yet finer scale eddies appear right near the singularly sharp lip. These eddies do not appear to much alter the peak heating near the base of the reattachment shock.

Figure 16: Mean heat flux distribution on outside of body for various surface spacings to determine grid convergence
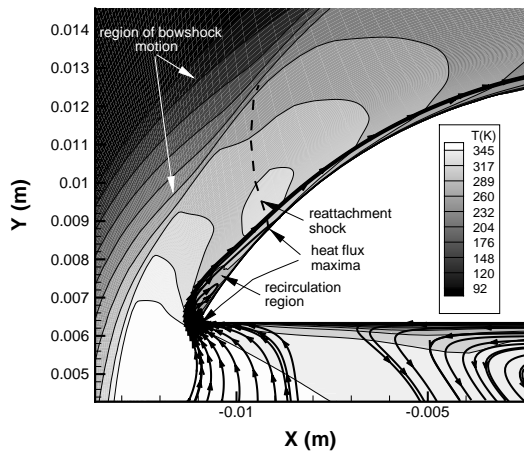

Figure 15: Mean temperature contours with select streamlines in the vicinity of the sharp lip. Note that since the flow is highly oscillatory, major flow features such as the bow shock, the separated recirculation region, and the reattachment shock are blurred by the motion.

This grid (300 x 399 cells outside with 200 x 99 cells inside and surface cell fineness of $2.5 \times 10^{-4}mm$) with 4000 time steps per cycle was then used to determine the
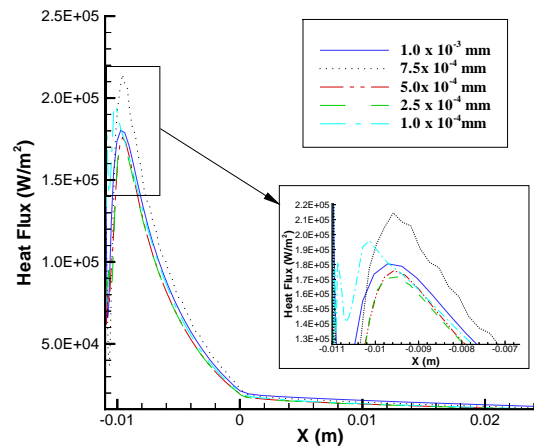
pseudo-steady solution for the case of an isothermal wall at $100K$. The mean surface heat flux distribution for this boundary condition was found to be adequately converged between the 98th and 99th cycle from the start of the calculations done at coarser temporal and spatial resolution. The mean surface heat flux (fig. 17) obtained from the 99th pressure oscillation cycle would therefore be used to calculate the heat conduction coefficient distributions that were to be input into the heat conduction code.

As expected ([4],[7]), figure 17(c) shows that there is a very low mean surface heat flux along the base wall of the cavity. The mean heat flux then increases along the cavity length to reach a peak value ($\sim 425,000W/m^2$) near the sharp lip at $x = -0.011m$ (fig. 17(b)). The mean heat flux again decreases along the outside of the body below the separation region, increases through the recirculation region to a local maximum at the reattachment shock ($-0.0105m \lesssim x \lesssim -0.0095m$), decreases rapidly to the shoulder of the body($-0.0095m \lesssim x < 0m$), and then tapers off to a negligible heat flux at the end of the nose tip model ($x > 0m$) (fig. 17(a)). These mean surface heat flux features were expected [4].

A nearly converged forced-steady adiabatic wall temperature distribution was used as the reference temperature to obtain the heat conduction coefficient distribution for the solid body heat conduction code so that preliminary solid body results could be obtained. It was found that the greatest temperature increase was at the cavity lip ($x = -0.0109m$) just inside the cavity. Figure 18 shows how the temperature of the solid at this point varies with time over a two second run. Two seconds was initially chosen based on the experimental results (sec. 4.2.2)which
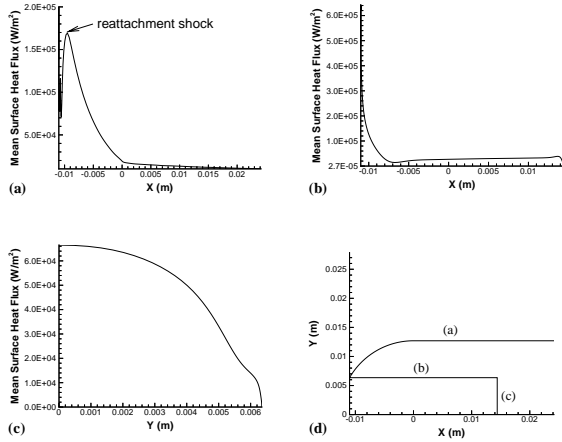
Figure 17: Mean heat flux distribution for isothermal wall at 100K along the (a) outside of body, (b) cavity top wall, (c) cavity base wall. (d) Schematic of body.

showed ablation onset occurring between 1 and 2 seconds for the sharp lip cases. The solid temperature did rise, but the very small temperature increase of only $\sim 12\,K$ that occurred even with very high heating at the lip suggests that there was a problem with the calculation.
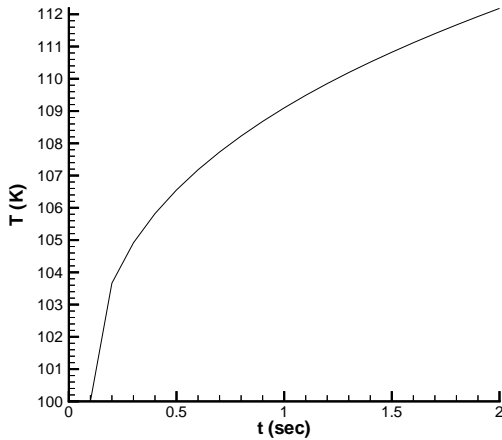

Figure 18: Temperature history for point of greatest temperature rise for the sharp lip cavity solid body calculated using $h(\theta, 100K)$.

It is presently unclear as to why a larger temperature increase is not found given the heating that is taking place at the surface. A more in depth study will be conducted once a converged, forced-steady, adiabatic wall temperature distribution is obtained.

4.1.2.2 Rounded Lip Separate temporal and spatial resolution studies were not conducted for the rounded lip cavity case because it was assumed that the sharp lip case, for which such studies were performed, was the more difficult case and that the resulting resolutions would be conservative for the rounded lip geometry. The results to date have only been obtained for a medium resolution grid (axial surface wall spacing of $1.0 \times 10^{-1} mm$, radial surface wall spacing of $9.05 \times 10^{-4} mm$) and a reasonable time step ($\sim$4000 steps per cycle) because of the number of zones needed (4) to accurately resolve the rounded lip. Due to this limited resolution in space, the mean surface heat flux distributions were expected to be only qualitatively correct due to an insufficiently resolved thermal boundary layer.
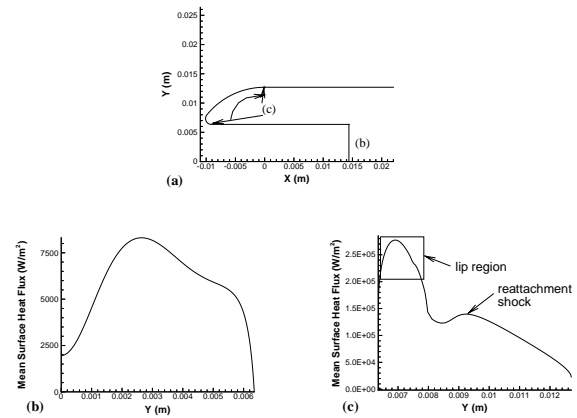

Figure 19: (a) Schematic of body. Unconverged mean heat flux distribution for isothermal wall at 100K along (b) cavity base wall, and (c) cavity lip, and outside of body.

The heat fluxes around the outside of the body (fig. 19(c)) appear lower than the heat fluxes for the sharp lip cavity case overall. The mean heat flux at the lip decreased by 35% to approximately $277,000 W/m^2$ which was expected [4]. The heat flux at the lip was still, however, slightly larger than that for the stagnation point of the baseline case which contrary to expectation [4, 13]. The elevated heat flux is likely due to the inaccurate resolution in space or the use of an insufficiently blunt lip. A peak heating point on the outside of the body again occurs at the reattachment shock with a mean heat flux of approximately $140,000 W/m^2$, which is almost 18% less than that for the sharp lip case.

The increase in heat flux at the middle of the cavity base wall (fig. 19(b)) was attributed to an under-resolved thermal boundary layer and a hot spot in this area that had not yet been expelled from the cavity from startup. The approach of the heat flux to zero at the top of the base wall was expected due to the concave shape of that corner. The heat flux distribution along the cavity base wall is expected

to become more consistent with that of the sharp lip cavity case once a converged solution is obtained. The heat conduction code has not been run at this time since a forced-steady adiabatic wall temperature solution has not yet been obtained due to problems within INCA.

4.2 Experimental Results

This study was limited to investigating the effect of the ratio of the cavity depth to the cavity diameter (L/D) and the cavity lip radius on the onset time of and the rate of ablation. Other parameters that may have influenced the results (including the ratio of cavity diameter to nose diameter, cavity lip shape, cavity base shape, and Reynolds number) have been examined by Yuceil and Engblom [13, 4] in relation to their effect on surface heating, not ablation.

Much of the present study focused on the baseline case and a deep cavity geometry (L/D = 2.0) that was found to self-sustain bow shock oscillations (Engblom [4]) and had a great effect on surface heating [13, 4]. Three shallower cavities (L/D = 0.25, 0.5, 1.0), which were found [3] to have cool recirculation regions at the nose tip were also examined, though in less detail. The present experimental findings will be separated into three sections below: baseline model (sec. 4.2.1), deep cavity model (sec. 4.2.2), and shallow cavity models (sec. 4.2.3). A synthesis of the findings is presented in section 4.2.4.

4.2.1 Baseline Model

Three separate wind tunnel runs were conducted for the baseline model in order to assess the repeatability of the results. The stagnation point may not be the first point to begin melting. The sides of the model (near $\theta \sim 45°$) may melt first and/or more quickly, as a cusped shape begins to form. This phenomenon is quite noticeable from viewing the time lapse photos (figs. 20(a) -(f)). The cusped shape phenomenon was also seen by Reinecke and Sherman [9] in their numerical ablation and shape change calculations and by Reinecke and Guillot [10] in their arcjet experiments. They believed the shape change was caused by boundary layer transition near the sonic point. The heat transfer below the turbulent boundary layer is very large, larger than at the stagnation point, and therefore the material will first ablate near the boundary layer transition point. Due to the similarities in shape change, boundary layer transition was also thought to drive the generation of a cusped shape in the current experiments. In the present experiments, small protruding glass fibers, natural transition, a noisy free stream, or a rim on the model due to an imperfect mold gap may have forced boundary layer transition.

The change in position of the stagnation point over time is seen in figure 21. The scatter that was present corresponds to errors in reading the exact pixel corresponding to

| (a) t = 0 sec | (b) t = 4.04 sec |

| (c) t = 7.94 sec | (d) t = 12.08 sec |

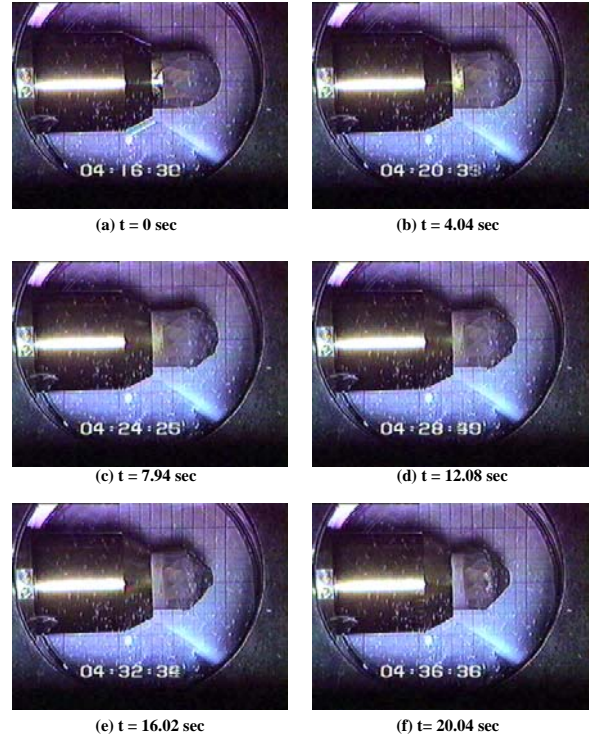| (e) t = 16.02 sec | (f) t= 20.04 sec |

Figure 20: Time lapse pictures of baseline case no. 1 from initial removal of shielding ($t = 0s$) through end of run ($t = 20s$). Time after removal of shielding is indicated under each picture.

the actual stagnation point. The differences in the lengths of the runs (seen by the difference in the number of data point for each run in figure 21) were due to how far into the tunnel run the shielding was removed. However, the differences in the shield removal time did not appear to have effected ablation onset time or rate as there was good agreement between the three runs.

The curve slopes (recession rates) of the stagnation point for each run were determined using data points from the estimated time at which melting began (4 seconds) on. The recession rates are fairly constant between runs (3%) as can be seen from the three least square fit lines on figure 21 and the actual recession rates (table 2). The average recession rate at the stagnation point was 0.294 mm/sec. The time at which melting began for each run was then calculated using the appropriate curve fit. The calculated times were slightly higher ($\sim$5 seconds, table 2) than the estimated times from which the curve slopes were determined, but not enough to warrant the recalculation of the curve fits. Differences between the numerically simulated time (table 1) and the experimentally calculated time for the onset of ablation were believed to be due to systematic errors associated with shield removal, inconsistent initial temperatures, etc.
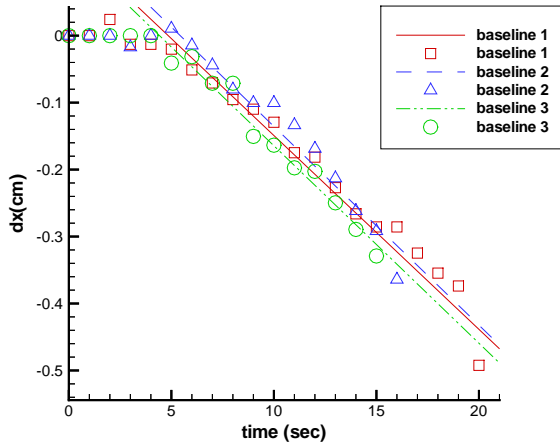
12

Figure 21: Stagnation point position versus time for three repeated baseline cases. Symbols with no line are for times prior to the presumed onset of ablation. Lines are least square linear fits of the data points after the onset of ablation.

	run 1		run 2		run 3	
	rate	time	rate	time	rate	time
L/D = 0	0.289	4.8	0.297	5.4	0.295	4.4
L/D = 2.0	0.413	1.6	0.464	1.1	0.460	4.2

Table 2: Recession rates and time at which ablation begins for baseline runs at the centerline and L/D = 2.0 experimental runs. All recession rates (rate) are in mm/s and ablation onset time (time) in seconds.

4.2.2 Deep Cavity Model

Three separate wind tunnel runs were conducted for the L/D = 2.0, deep cavity model to assess repeatability and to vary the lip radius. With a deep cavity in the model, visual ablation began at the most forward point on the lip of the model. Figures 22(a)-(f) show time lapse images from run 1 (sharp lip). One notices the jaggedness of the cavity lip as it begins to ablate and that ablation does not remain symmetric throughout the run. Again, this could be due to inconsistencies in the ice model. It was interesting to note that ice was still present over the entire interior of the cavity at the conclusion of the runs indicating very little heating at the cavity base. Also visible in the video were hints of shock motion confirming that shock oscillations were present.

Due to the jaggedness of the cavity lip an average model lip position was used to compare the runs. The change in this average position over time is shown in figure 23. Note

(a) t = 0 sec   (b) t = 2.98 sec

(c) t = 5.98 sec   (d) t = 9.01 sec
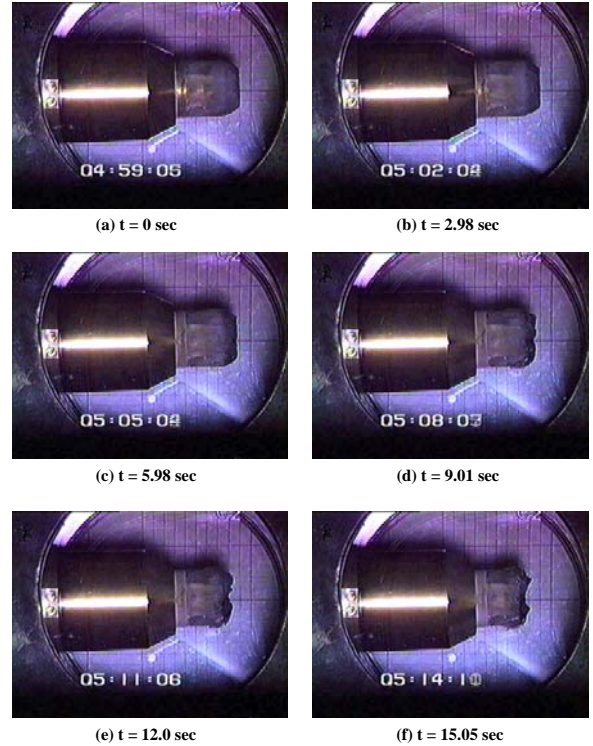
(e) t = 12.0 sec   (f) t = 15.05 sec

Figure 22: Time lapse pictures of L/D=2.0 cavity case, run 1, from initial removal of shielding (t = 0 sec) through end of run (t = 15 sec). Time after removal of shielding indicated under image.

that in run 1 the model had a sharp cavity lip while in runs 2 and 3, the cavity lip was rounded (∼1 mm). Agreement between runs was not as good as for the baseline case both in terms of the recession rate and the time of ablation onset. This could be due to the geometrical differences (i.e. cavity lip radius) between runs. Difference could also be due to the shielding coming off in an irregular manner between the runs, the fibers at the cavity lip interfering with the ablation, uncertain initial model temperature, the model being at a slight angle of attack, or defects in the model, though these would apply to the baseline runs, too.

The recession rates appeared roughly constant over time (fig. 23). A least square linear fit of the position data was again used to obtain the average recession rate of each run. The average recession rate for all three L/D=2.0 cavity runs was approximately 0.445 mm/sec, nearly twice as fast as for the baseline blunt model. The onset of ablation appeared to occur at approximately one to two seconds, except in run three where ablation onset was delayed to four seconds. The rounded lip in run 3 was formed with the sandpaper on the drill press while the rounding of the lip in run 2 was done entirely by hand. The lip in run 3 was more uniformly rounded, which would have been a cause for the
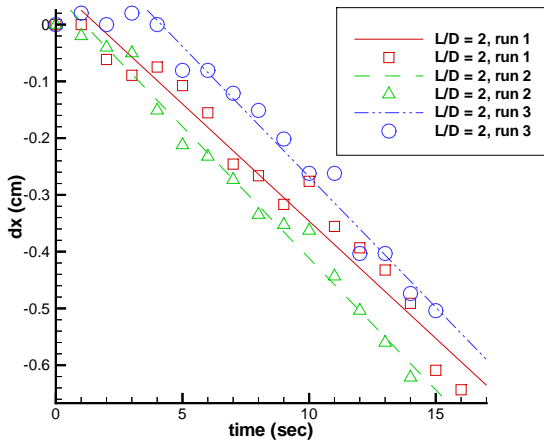
13

Figure 23: Average nose tip position versus time for L/D=2.0 cavity cases. Lines are least square linear fits of the data points after the onset of ablation.
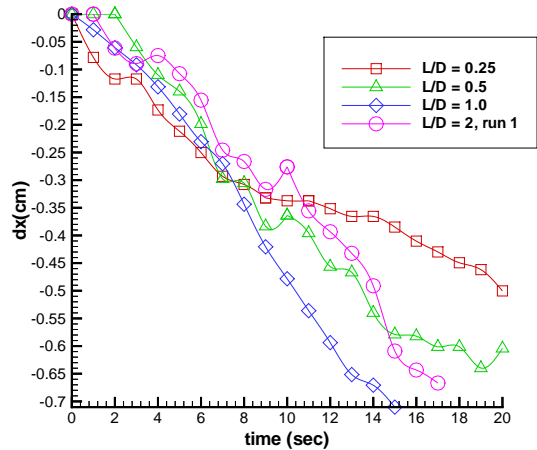

Figure 24: Position versus time plots for the three shallow, sharp lip cavity cases and the one deep, sharp lip cavity case. Note obvious changes in slope of data points at 6-9 seconds.

delayed ablation onset. The sharp lip model in run 1 began ablating rapidly after about 1 sec. This would be expected, as the heating near the lip would be severe [4, 13].

4.2.3 Shallow Cavity Models

One wind tunnel run was conducted for each shallow cavity model (L/D = 0.25, 0.5, 1.0) to determine trends. All three cases had sharp lip cavities.

The ice leading edge positions versus time are seen in figure 24. The three shallow models show interesting trends. While the different models appear to start ablating at approximately the same time and rate, the rates begin to differ after a few seconds into the run. The shallowest cavity's (L/D = 0.25) recession rate appears to slow down first at about t = 9 sec, while the L/D = 0.5 rate slows down later (∼t = 15 sec) and the L/D = 1.0 case does not appear to slow its recession rate at all. The change in recession rate appears to be correlated with the time at which the cavity has completely ablated away. That is, the L/D=0.25 cavity was 0.3 cm deep while the L/D=0.5 cm cavity was 0.6 cm deep.

4.2.4 Effect of L/D

As expected, introducing a forward facing cavity into the nose tip of a projectile did change the ablation rate. While deeper cavities seem to have slower ablation rates than shallower cavities, the ablation rate of the stagnation point of the baseline case is nearly two times slower yet. The onset of ablation also appeared to occur later for the stagnation point of the baseline case than for any of the cav-

ity cases, but was very close to the time of the blunt-lip L/D=2.0 run (case 3). The expected delay in the onset of ablation may not have been observed because a sufficiently deep cavity may not have been utilized in this experiment. It is also possible that the cavity lips were not sufficiently rounded which would also have caused an earlier onset of ablation.

The effect of only cavity depth is illustrated by figure 24 which includes the sharp lip, deep cavity case along with the shallower, sharp lip cavity cases. The trends of the sharp lip, deep cavity case tend to agree better with the other sharp lip cases, although they were shallow cavities, than with the other deep cavity cases. Therefore, it is thought that lip radius has a strong effect on ablation. In fact, Engblom [4] found that rounding the lip was necessary in order to reduce the local surface heating since the air flow into the cavity directly impinges on the cavity lip. Based on these findings, it is believed that there is an optimum lip radius at which heating will be minimized subject to other constraints. It is likely that a highly blunted lip will have a longer delay in the onset of ablation.

5 Discussion

5.1 Numerical and Experimental Comparison

Numerical and experimental results compare surprisingly well for the baseline case. The numerical results predicted ablation onset at approximately 4 seconds. The experimen-

tal results confirmed ablation onset at 4-5 seconds.

The presence of ice in the cavity after the completion of the deep cavity experiments confirms the low heating at the base of the cavity that was predicted by the numerical emulation. Assuming that agreement is as good between the numerically predicted onset of ablation, once completed, and the experimental results for the deep cavity case, using the numerical emulation to obtain future results should not be a problem.

5.2   Computations

A numerical procedure has been developed to allow the flowfield and solid body computations to be solved independently with linked boundary conditions. Based on the complete results of the baseline study, it is believed that only a few iterations between the flowfield code and the solid body heat conduction code are needed to obtain adequate results.

Most of the assumptions that were made for the flowfield calculations appear to have been reasonable except for the assumption of laminar flow. Although numerical results appear reasonable based on experimental findings for the baseline body where the stagnation point flow probably was laminar, the experimental results suggest that the flow is transitioning near the sonic line on the baseline body.

The use, to date, of a forced-steady adiabatic wall temperature distribution to compute the heat conduction coefficients used in the heat conduction procedure needs to be examined. Although potentially quicker to obtain, the forced-steady distribution may not give results as accurate as would be obtained using the mean adiabatic wall temperature distribution averaged over one unsteady oscillation cycle.

The assumption made in the solid body heat conduction code of constant material properties probably needs to be revisited because of the range of temperatures over which the investigation occurred ($78K - 273K$). In this range, for example, the thermal conductivity of ice varies from approximately $7.5W/mK$ at $78K$ to $2.22W/mK$ at $273K$. Only the material properties at $273K$ were assumed in the present study.

To date, a complete set of numerical results has only been obtained for the baseline case. These results, heat flux distribution and ablation onset time, appear reasonable.

Accurate results for the sharp lip cavity case have only been obtained for the heat flux distribution at $100K$. Preliminary solid body heat conduction results have been obtained using a nearly converged forced-steady adiabatic wall temperature distribution as the reference temperature. The preliminary results, however, do not appear reasonable. It is unclear based on the present data what the cause of this inaccuracy was although it may have to do with res-

olution or a problem with INCA.

The heat flux distributions for the rounded lip case appear reasonable, but a bit high, around the outside of the body. As expected [4, 13], the heating at the lip has been significantly reduced by rounding the lip. However, the trends along along the cavity base wall do not appear accurate at this time perhaps because the thermal boundary layer is not well resolved at the base wall. An inaccurate solution along the base wall should not have much effect on the solid body heating since the magnitude of the heat flux is expected to remain small even when the flow is accurately resolved. If the current heat flux distribution was used as input for the heat conduction code, then the ablation onset would be expected to occur later than for the sharp lip case since the overall peak heating is less. However, a converged, forced-steady adiabatic wall temperature distribution for the rounded lip case must be obtained before the heat conduction code can be run.

Overall, the viability of using the numerical model for unsteady cavity flows cannot be confirmed until certain problems with the cavity geometries can be eliminated. Initial results (baseline ablation onset time and cavity lip heat flux values), however, appear promising.

5.3   Experiment

The experimental method also looks promising, although some of the results are unexpected. The shielding appears to protect the ice model during wind tunnel startup, though temperature rise of the ice prior to exposure remains to be investigated. The mold appears versatile enough to accommodate a number of different geometries without much modification. Water ice seems to work well as a low temperature ablator; it could easily be formed to the desired shapes.

The results for the baseline case were consistent. The discrepancies between deep cavity runs need to be investigated further. It remains uncertain why ablation onset occurs earlier in the L/D=2, round lip case than the baseline case for what was thought to be a sufficiently deep cavity based on results by Engblom [4]. One possibility may be that the flow is transitioning from laminar to turbulent as it leaves the cavity; this would increase surface heating. The sharp lip cavity cases (both shallow and deep) appeared to have similar ablation onset times and initial ablation rates. The sharp lip is therefore believed to negate any beneficial effect of a deeper cavity. However, the onset of ablation seems to be delayed and ablation rates decreased with increased cavity lip radius for the deep cavity case.

Even after viewing the experimental results for the cavity cases, it is unclear whether flow was transitioning around the body. If flow was transitioning or completely turbulent as it left the cavity, then the fact that the experimental

results for the L/D=2.0 rounded lip case (run 3) showed ablation onset at approximately 4 seconds, suggests that the cooling mechanism does indeed work. That is, turbulent flow causes greater heating of a body than does laminar flow, so if flow was turbulent as it left the cavity one would expect ablation onset to occur earlier than for a laminar flow. Therefore, an ablation onset at approximately the same time for a turbulent cavity case and a laminar baseline blunt body case would suggest that the use of a cavity to induce oscillations can indeed decrease the heating and delay the onset of ablation.

Acknowledgments

References

[1] Engblom, W.A. and Goldstein, D.B., "Nose-Tip Surface Heat Reduction Mechanism," *J. of Thermophysics and Heat Transfer*, Vol. 10, No. 4, pp. 598-606, Oct.-Dec. 1996.

[2] Engblom, W.A., Goldstein, D.B., Ladoon, D., and Schneider, S.P., "Fluid Dynamics of Hypersonic Forward-Facing Cavity Flow," *J. of Spacecraft and Rockets*, Vol. 34, No. 4, pp. 437-444, July-Aug. 1997.

[3] Engblom, W.A., Yuceil, B., Goldstein, D.B., and Dolling, D.S., "Experimental and Numerical Study of Hypersonic Forward-Facing Cavity Flow'," *J. of Spacecraft and Rockets*, Vol. 33, No. 3, May-June 1996.

[4] Engblom, W.A., Numerical Investigation of Hypersonic Flow Over a Forward-Facing Cavity, University of Texas at Austin, PhD Dissertation, Aug. 1996, pp. 20-29, 36, 41, 122-125, 128-143.

[5] Farnsworth, S. and Wilson, D.E., "A Preliminary Investigation of the Helmholtz Resonator Concept for Heat Flux Reduction Part I: Experimental Program," IAT.P 0024, Institute for Advanced Technology, The University of Texas at Austin, Oct. 1992.

[6] Fay, J.A. and Riddell, F.R., "Theory of Stagnation Point Heat Transfer in Dissociated Air," *J. of the Aeronautical Sciences*, Vol. 25, No. 2, Feb. 1958.

[7] Huebner, L.D. and Uteja, L.R., "Experimental Flowfield Measurements of a Nose Cavity Configuration," SAE Paper 871880, Oct. 1987.

[8] Mills, A.F., *Heat Transfer*, Irwin, Boston, MA 1992.

[9] Reinecke, W.G. and Guillot, M.J., "Full Scale Ablation Testing of Candidate Hypervelocity Nose Tip Materials," Proceedings of the 15th International Symposium on Ballistics, May 1995.

[10] Reinecke, W.G. and Sherman, M., "Tip Survivability and Performance on Hypervelocity Projectiles," Proceedings of the 14th International Symposioum on Ballistics, Sept. 1993.

[11] Yuceil, B, Dolling, D.S., and Wilson, D., "A Preliminary Investigation of the Helmholtz Resonator Concept for Heat Flux Reduction," AIAA Paper 93-2742, July 1993.

[12] Yuceil, B. and Dolling, D.S., "Effects of a Nose Cavity on Heat Transfer and Flowfield Over a Blunt Body at Mach 5," AIAA Paper 94-2050, June 1994.

[13] Yuceil, B., An Experimental Investigation of a Forward-Facing Nose Cavity on a Blunt Body at Mach 5, University of Texas at Austin, PhD Dissertation, Dec. 1995, pp. 77-94, 123-132.

[14] Yuceil, B. and Dolling, D.S., "IR Imaging and Shock Visualization of Flow over a Blunt Body with a Nose Cavity," AIAA Paper 96-0232, Jan. 1996.